

MUSE: Resolving Manifold Misalignment in Visual Tokenization via Topological Orthogonality

Panqi Yang¹ Haodong Jing¹ Jiahao Chao² Tingyan Xiang² Li Lin² Yao Hu² Yang Luo² Yongqiang Ma¹

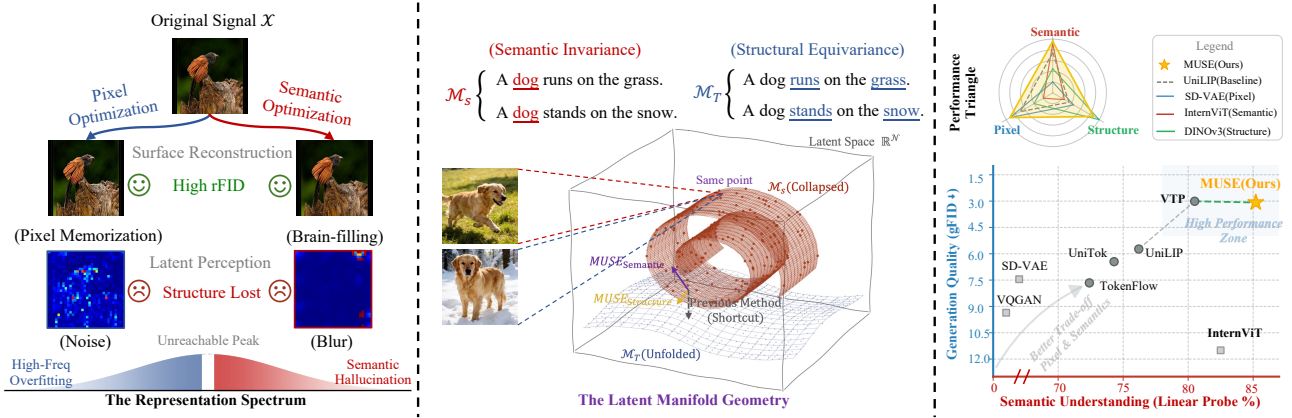


Figure 1. Breaking the Visual Tokenization Trade-off via Manifold Unification. (a) **Perceptual Polarization:** Existing unified tokenizers (Ma et al., 2025; Tang et al., 2025) reconstruct images well, but their representations remain polarized: pixel supervision favors fragmented high-frequency details, while semantic supervision yields blurry abstractions, leaving mid-frequency structures under-modeled. (b) **Manifold Misalignment:** Naively combining pixel and semantic objectives causes destructive interference: pixel gradients unfold the manifold for detail, whereas semantic gradients collapse it for invariance, resulting in a zero-sum trade-off. (c) **Topological Orthogonality:** MUSE uses structure as an orthogonal bridge, anchoring semantics in feature values and geometry in attention topology. This decouples conflicting objectives and enables mutual reinforcement.

Abstract

Unified visual tokenization faces a fundamental trade-off between high-fidelity pixel reconstruction (spatial equivariance) and semantic abstraction (conceptual invariance). We attribute this conflict to *Manifold Misalignment*: naive joint optimization induces opposing gradients, creating a zero-sum game between reconstruction and perception. To address this, we propose **MUSE**, a framework based on *Topological Orthogonality*. By treating *Structure* as an orthogonal bridge, MUSE decouples optimization within Transformers: structural gradients refine attention topology, while semantic gradients update feature

values. This turns destructive interference into *Mutual Reinforcement*. Experiments show that MUSE breaks the trade-off, achieving state-of-the-art generation quality (gFID 3.08) and surpassing its teacher InternViT-300M in linear probing (85.2% vs. 82.5%), demonstrating that structurally aligned reconstruction can enhance semantic perception. Code is available at [GitHub](#).

1. Introduction

The success of Large Language Models (LLMs) has driven unified modeling into multimodal domains, aiming to bridge the architectural gap between image understanding and generation. Traditionally, these tasks have relied on different paradigms: understanding models align CLIP-like (Radford et al., 2021) semantic encoders with LLMs (Bai et al., 2025), while generative models employ diffusion latents (Xie et al., 2024a) or discrete VQ-VAE tokens (Van Den Oord et al., 2017). To bridge this gap, recent research has focused on developing a **Unified Visual Tokenizer** as a common interface for both understanding and generation. Recent pioneering

¹State Key Laboratory of Human-Machine Hybrid Augmented Intelligence, National Engineering Research Center of Visual Information and Applications, and Institute of Artificial Intelligence and Robotics, Xi'an Jiao Tong University ²Xiaohongshu Inc. Correspondence to: Yongqiang Ma <musayq@xjtu.edu.cn>.

works, such as UniTok (Ma et al., 2025), TokenFlow (Qu et al., 2025), and UniLIP (Tang et al., 2025), attempt to integrate these capabilities within a single codebook or latent space. However, despite their architectural unification, these approaches remain trapped in a **Zero-Sum Game** between reconstruction and understanding. By passively balancing high-frequency pixel details against low-frequency semantic abstractions, they fail to achieve true **Mutual Reinforcement**. Consequently, these models often trade off semantic alignment for generative fidelity, failing to achieve the perception-generation synergy required for a truly unified multimodal framework.

To identify the root cause of the trade-off, we analyze the perceptual divergence in existing unified approaches, as detailed in Figure 1(a). While these methods achieve high-fidelity reconstruction, their internal representations suffer from **Perceptual Polarization**. Specifically, pixel-level optimization (e.g., in VA-VAE (Yao et al., 2025b)) drives attention towards a *Fragmented View*, scattering focus across high-frequency textures while failing to capture structural coherence. Conversely, semantic alignment (e.g., in UniLIP (Tang et al., 2025)) forces a *Blurry View*, aggressively filtering out spatial details to satisfy invariance constraints. This gap between perceptual extremes reveals a “missing middle”: neither objective captures **Structure**, the inherent structural information characteristic of self-supervised models like DINO (Siméoni et al., 2025). This observation leads to our core insight: *Could structural cues serve as the critical bridge to reconcile the conflict between pixel fidelity and semantic abstraction?*

To better understand how “structure” can bridge this gap, we propose to view the optimization challenge through the lens of manifold geometry, as illustrated in Figure 1 (middle). From this perspective, the goals of understanding and generation can be conceptualized as two distinct geometric needs: (1) **Semantic Invariance** (\mathcal{M}_S), which encourages the latent space to “collapse” unnecessary variations (like changing backgrounds) so that concepts remain stable; (2) **Structural Equivariance** (\mathcal{M}_T), which requires the space to remain “unfolded” to preserve the spatial layout and pose details essential for reconstruction. This geometric framing reveals the heart of the conflict: semantic alignment tries to *compress* the space to extract meaning, while pixel reconstruction tries to *expand* it to cover details. When we try to optimize both in a shared space without separation, these opposing forces: one pulling in, the other pushing out result in what we term *Manifold Misalignment*, leading to the destructive interference observed in existing methods.

In this paper, we propose **MUSE** (Manifold Unification via Structural Embedding) to resolve this geometric deadlock. To reconcile the opposing dynamics of “compressing” for semantics and “expanding” for structure, we propose the

Gradient Orthogonality Hypothesis, which posits that semantic and structural objectives can be decoupled into non-interfering subspaces. We instantiate this principle through **MUSE**: mapping content to *Feature Values* and geometry to *Attention Topology*, and empirically verify the validity of this hypothesis, demonstrating that these objectives indeed reside in orthogonal parameter domains.

We instantiate this via the **Synergistic Block**, an architecture that decouples gradient flow into non-interfering pathways. It routes semantic gradients to update feature values via *Active Semantic Anchoring* and structural gradients to refine attention topology via *Structural Topology Alignment*. By structurally isolating these manifolds, MUSE transforms interference into synergy, allowing semantics and reconstruction to mutually reinforce each other.

Extensive experiments show that MUSE sets a new pareto frontier. As a tokenizer, it breaks the zero-sum game, matching specialist generation fidelity (gFID 3.08) while excelling in understanding (MMVP 74.8). When integrated into Unified Multimodal Models (UMMs), it enables high-quality generation and editing without compromising perception. Our contributions are:

- We identify **Manifold Misalignment** as the root cause of the trade-off between understanding and generation, showing that pixel and semantic objectives produce conflicting gradients during joint optimization.
- We propose **MUSE**, which resolves the conflict via **Topological Orthogonality**. It physically decouples optimization by anchoring semantic invariance in feature values and structural equivariance in the attention topology, thereby eliminating gradient interference.
- We achieve genuine **Mutual Reinforcement**. Uniquely, MUSE outperforms its own teacher backbone in linear probing (85.2% vs. 82.5%), proving that structurally aligned reconstruction actively refines rather than dilutes semantic perception.

2. Related Work

Visual Tokenization for Generation. The cornerstone of visual generation lies in mapping high-dimensional pixels to compact latent codes. Foundational works like VQ-VAE (Van Den Oord et al., 2017) and VQGAN (Esser et al., 2021) established the paradigm of discrete quantization with adversarial training to capture the *Texture Manifold*. Subsequent research has significantly scaled these architectures: ViT-VQGAN (Yu et al., 2021) and MagViT (Yu et al., 2023a;b) introduced Transformer-based codebooks for high-fidelity video synthesis, while methods like TiTok (Yu et al., 2024) and LFQ (Mentzer et al., 2023) explored 1D tokenization for extreme compression. More recently, autoregressive priors

have been refined by scale-wise generation in VAR (Tian et al., 2024) and continuous-valued modeling in MAR (Li et al., 2024b) and LlamaGen (Sun et al., 2024). Despite their photorealistic reconstruction, these generation-centric tokenizers suffer from “semantic blindness” (Tong et al., 2024); optimizing heavily for high-frequency pixel details often results in a latent space that neglects the abstract concepts required for robust understanding.

Visual Representation Learning. Conversely, representation learning prioritizes the *Semantic* or *Structural Manifold*. Contrastive language-image pre-training, exemplified by CLIP (Radford et al., 2021), ALIGN (Li et al., 2021), and SigLIP (Zhai et al., 2023), aligns visual features with text to enable zero-shot comprehension. Parallely, Masked Image Modeling (MIM) approaches like MAE (He et al., 2022) and BEiT (Bao et al., 2021) learn structural representations via reconstruction. A distinct category involves self-supervised distillation methods such as DINO (Caron et al., 2021), which capture intrinsic object geometry and part-whole relationships through attention mechanisms. While semantically rich, these discriminative representations are inherently lossy regarding texture (Li et al., 2024a), preventing their direct use as decodable tokens for generation.

Unified Visual Tokenization. To bridge the schism between generation and understanding, recent research pursues unified architectures. Generalist models like Chameleon (Team, 2024), Transfusion (Zhou et al., 2024), Emu3 (Wang et al., 2024), and UniTok (Ma et al., 2025) integrate modalities into a single sequence; yet, they often resort to separate or sub-optimal codebooks. To enhance cross-modal alignment, methods such as SEED-X (Ge et al., 2024), LWM (Liu et al., 2024), Show-o (Xie et al., 2024b), AToken (Lu et al., 2025) and TokenFlow (Qu et al., 2025) introduce mechanisms ranging from causal Q-Formers to unified flow objectives, while Tuna (Liu et al., 2025) further refines this alignment through connective token tuning. More aggressive approaches, including UniLIP (Tang et al., 2025), VTP (Yao et al., 2025a), Ming-UniVision (Huang et al., 2025), Janus (Wu et al., 2025a), and RecTok (Shi et al., 2025), explicitly distill semantic supervision (e.g., from CLIP) into the tokenizer. However, we argue that the naive weighted sum of these objectives forces a zero-sum trade-off. The resulting gradient conflicts between pixel reconstruction and semantic abstraction prevent true mutual reinforcement, where structure and generation should actively facilitate each other.

3. Problem Formulation

We frame visual tokenization as a multi-objective optimization under *manifold misalignment*, where generation and understanding impose conflicting geometric constraints. This section motivates the architectural design of MUSE.

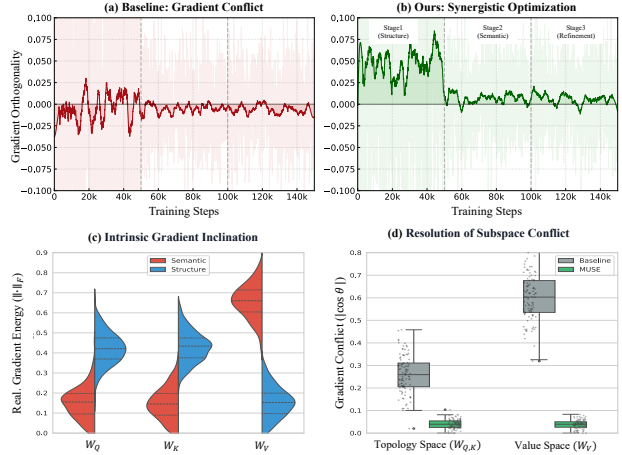


Figure 2. Verification of Manifold Orthogonality. (a-b) **Dynamics:** Naive optimization suffers from gradient conflict (negative cosine), whereas MUSE enforces orthogonality, transforming friction into synergy. (c-d) **Mechanism:** Split violin plots reveal that semantic gradients naturally occupy W_V while structural ones occupy $W_{Q,K}$. MUSE respects this inductive bias, eliminating the high-variance interference in W_V that plagues baselines.

3.1. Manifold Misalignment: Semantics vs. Topology

Let \mathcal{X} denote the observation space and \mathcal{Y} denote the semantic space. A tokenizer learns a mapping $f_\theta : \mathcal{X} \rightarrow \mathcal{Z}$. We posit that an ideal latent representation Z must satisfy two distinct properties, corresponding to two underlying manifolds. First, **Semantic Invariance** (\mathcal{M}_S): Z must capture abstract concepts robust to nuisance factors (e.g., lighting, texture). Second, **Structural Equivariance** (\mathcal{M}_T): Z must preserve the intrinsic *relational geometry* of the scene, such as the adjacency and spatial layout of object parts.

The core conflict arises because standard reconstruction objectives force Z to approximate the high-frequency surface of the pixel space \mathcal{X} , shown in Figure 1(middle). This optimization vector is often orthogonal to the gradients required for the low-frequency \mathcal{M}_S . Consequently, optimizing solely for pixel fidelity erodes semantic alignment, while pure semantic optimization results in structural collapse.

3.2. Structural Information Decomposition

To resolve this, we maximize the mutual information $I(Z; X, Y)$ by introducing a latent variable S representing the **Structural State**, a sufficient statistic for the intrinsic geometry of \mathcal{X} . Assuming a dependency where structure acts as the prerequisite for semantics ($Y \leftarrow S \rightarrow X$), we decompose the objective via the chain rule:

$$I(Z; X, Y) \approx I(Z; S) + I(Z; Y|S) + I(Z; X|S, Y). \quad (1)$$

This factorization necessitates a prioritized optimization strategy. The first term, $I(Z; S)$, serves as the **Geomet-**

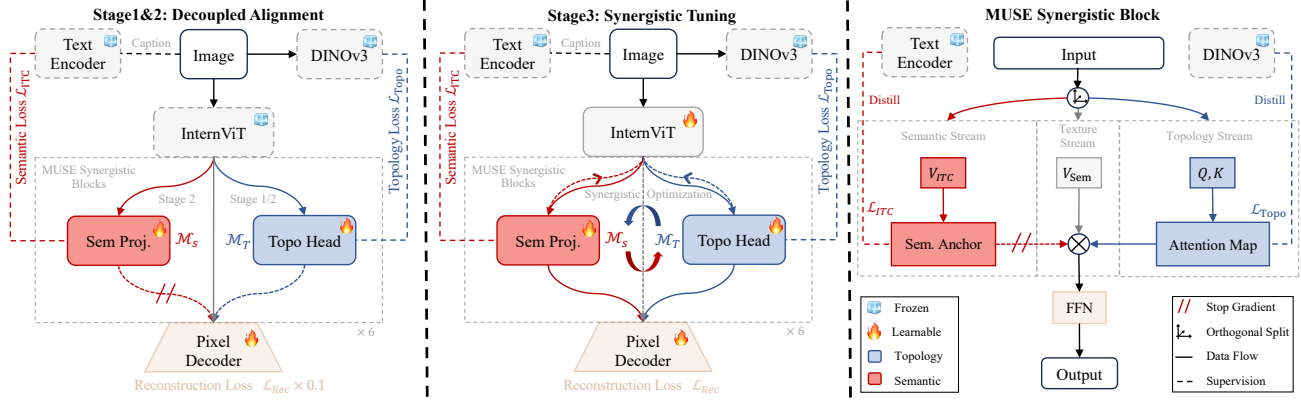


Figure 3. **The MUSE Framework: Overview of Training Stages and Synergistic Architecture.** **Left–Middle.** MUSE is trained in three stages. **Stage 1: Topology warmup** aligns the encoder’s attention topology with a self-supervised teacher using the Structural Topology Alignment loss \mathcal{L}_{topo} (encoder frozen). **Stage 2: Semantic injection** anchors token values to the vision–language manifold via \mathcal{L}_{ITC} while preserving the learned topology. **Stage 3: Synergistic tuning** unfreezes the backbone for end-to-end integration with reconstruction. **Right.** We decouple *structure* and *semantics* into orthogonal subspaces of a Transformer layer: structural gradients update routing parameters (W_Q, W_K) to shape the attention graph A , while semantic gradients update value parameters (W_V) to encode content. A stop-gradient operator ($//$) isolates the semantic branch from reconstruction gradients, effectively decoupling the conflict between understanding and reconstruction.

ric Foundation, anchoring Z to the topological manifold \mathcal{M}_T . The second term, $I(Z; Y|S)$, represents **Semantic Injection**. It implies that, conditioned on the established structural topology, Z must be populated with semantic concepts Y . This mathematically justifies our curriculum of prioritizing structural alignment before semantic optimization, details in Section 4. The final term, $I(Z; X|S, Y)$, represents residual texture details, which can be delegated to the decoder, thereby relieving the encoder from memorizing high-frequency noise.

3.3. The Gradient Orthogonality Hypothesis

To resolve manifold misalignment, we propose that the conflict between semantics and structure stems from parameter entanglement rather than intrinsic task incompatibility. By leveraging the architectural properties of a Transformer block, we formulate the **Gradient Orthogonality Hypothesis**, which posits that these objectives can be reconciled by decoupling updates into the distinct subspaces of **Feature Values** (W_V) and **Attention Topology** ($W_{Q,K}$). Our analysis in Figure 2 substantiates this conjecture, revealing an *Intrinsic Functional Specialization* where semantic gradients naturally concentrate in W_V while structural ones cluster in $W_{Q,K}$ (Figure 2c). Standard optimization ignores this bias and forces competing gradients into shared domains, leading to severe *destructive interference* evidenced by significant negative cosine similarity ($\cos \theta_g \ll 0$, Figure 2a). By explicitly routing gradients to their native subspaces, MUSE enforces orthogonality to bring the cosine similarity to near-zero ($\cos \theta_g \approx 0$, Figure 2d), effectively transforming optimization friction into synergistic mutual reinforcement.

4. Method: MUSE

We propose **MUSE**, a framework designed to physically instantiate the information-theoretic decomposition derived in Section 3. To resolve the fundamental *Manifold Misalignment* between reconstruction and understanding, MUSE abandons the conventional monolithic encoding strategy, which entangles conflicting gradients. Instead, it implements *Topological Orthogonality* by explicitly decoupling the optimization of high-level semantics (anchored in feature values) and structural geometry (anchored in attention topology) within a unified Transformer architecture. This design effectively transforms the destructive interference of competing objectives into a mechanism of *mutual reinforcement*.

4.1. Synergistic Architecture Design

The cornerstone of our framework is the **Synergistic Block**, a specialized Transformer layer engineered to satisfy the *Gradient Orthogonality Hypothesis*. Unlike standard layers that entangle semantic content and geometric structure in a single mixing process, the Synergistic Block processes them via bifurcated functional pathways sharing a common residual backbone.

Formally, let $H_l \in \mathbb{R}^{N \times D}$ denote the input features to layer l . We decompose the self-attention mechanism to physically isolate the structural subspace from the value subspace. First, the **Topology Stream** computes the adjacency matrix A , which encodes the geometric relationships between tokens. This stream is parameterized by projection matrices W_Q and W_K , and is optimized exclusively by the structural

objective:

$$\begin{aligned} Q_{topo} &= H_l W_Q, & K_{topo} &= H_l W_K, \\ A &= \text{Softmax} \left(\frac{Q_{topo} K_{topo}^T}{\sqrt{d_k}} \right). \end{aligned} \quad (2)$$

Simultaneously, the **Semantic Stream** updates the feature content based on this established topology. It employs a separate projection W_V to compute V_{sem} , which is then aggregated via the structural map A :

$$V_{sem} = H_l W_V, \quad H_{attn} = A \cdot V_{sem}. \quad (3)$$

Crucially, by structurally separating the parameters governing *relationships* (W_Q, W_K) from those governing *content* (W_V), our method enables non-interfering parallel optimization. Gradients from the structural loss refine the routing logic (topology), while semantic gradients adjust the feature values (semantics), effectively realizing the orthogonality hypothesis in the parameter space.

4.2. Structural Topology Alignment

To maximize the foundational structural term $I(Z; S)$, the encoder must first capture the intrinsic geometry of the visual data. We posit that an optimal structural prior is latent in the attention maps of self-supervised models (e.g., DINOv3 (Siméoni et al., 2025)), which exhibit emergent object segmentation properties.

We propose a **Structural Topology Alignment** constraint, enforcing the student’s attention topology A_S to be isomorphic to the teacher’s structure A_T . Acknowledging that the student and teacher may operate at different resolutions, we apply a 4D-interpolation function $\Psi(\cdot)$ to align the spatial dimensions of the attention tensors. The objective is formalized as the KL divergence between the attention distributions, averaged over layers L and heads H :

$$\mathcal{L}_{topo} = \frac{1}{LH} \sum_{l=1}^L \sum_{h=1}^H D_{KL} \left(\Psi(A_T^{(l,h)}) \parallel A_S^{(l,h)} \right). \quad (4)$$

This loss explicitly targets the routing parameters (W_Q, W_K) in the Synergistic Block. It teaches the model how to look at objects by grouping pixels into coherent parts independent of semantic labels, thereby establishing the necessary geometric foundation for subsequent learning.

4.3. Active Semantic Anchoring

With the structural topology established, we proceed to maximize the conditional semantic term $I(Z; Y|S)$. We employ **Active Semantic Anchoring** to populate the geometric skeleton with abstract concepts. Existing methods (Tang et al., 2025) often rely on passive distillation, which is prone

to being overwritten by reconstruction gradients. In contrast, we treat semantic alignment as a dynamic manifold constraint.

We introduce a semantic projector $g_\phi(\cdot)$ that maps the pooled visual tokens \bar{z} into the joint vision-language space. Instead of standard retrieval objectives, we utilize the Noise Contrastive Estimation (NCE) (Ma & Collins, 2018) framework to impose a rigorous lower bound on the mutual information:

$$\mathcal{L}_{anchor} = \mathcal{L}_{NCE}(g_\phi(\bar{z}), t) \approx -I_{LB}(Z; Y|S), \quad (5)$$

where t represents the paired text embedding. This active supervision acts as a Lagrangian multiplier, firmly anchoring the feature values (V_{sem}) within the semantic manifold \mathcal{M}_S . This prevents the “semantic drift” phenomenon, ensuring that understanding capabilities are maintained even when optimizing for pixel reconstruction.

5. Experiment

5.1. Implementation Details

Architectures. We introduce two model variants, MUSE-1B and MUSE-3B, constructed by integrating InternVL3 (Zhu et al., 2025) with the SANA (Xie et al., 2024a). Specifically, MUSE-1B combines InternVL3-1B with SANA-0.6B, whereas MUSE-3B utilizes InternVL3-2B and SANA-1.6B. We directly employ the InternViT from InternVL3 as the visual encoder and adopt the pixel decoder from DC-AE (Chen et al., 2024). Our connector is composed of a stack of 6 synergistic blocks. For the learnable queries within the continuous tokenizer, we set $N = 256$.

Training Data. We utilize the BLIP3-o (Chen et al., 2025b), ImageNet-1K (Deng et al., 2009), and ADE20K (Zhou et al., 2017) datasets for tokenizer tasks. The pre-training corpus comprises approximately 36M samples, consisting of 27M images recaptured by Qwen2.5-VL-7B (Bai et al., 2025), 5M samples from CC12M (Changpinyo et al., 2021), and 4M synthesized images from JourneyDB (Sun et al., 2023). For instruction tuning, we employ 60K high-quality image-text pairs generated by GPT-4o (Hurst et al., 2024). Regarding image editing, we utilize the GPT-Image-Edit-1.5M dataset (Wang et al., 2025) for the pre-training phase. For the subsequent instruction tuning, we adopt ShareGPT-4o-Image (Chen et al., 2025a), which contains 46K editing samples, the same as UniLIP (Tang et al., 2025).

MUSE Tokenizer Training. We train the continuous tokenizer on the BLIP3-o corpus using 8 NVIDIA H20 GPUs (batch size 48). The training process is structured into three consecutive stages, each consisting of 50k steps. We employ a step-wise learning rate decay schedule: the first stage

Table 1. **Resolving Manifold Misalignment in Visual Tokenization.** Quantitative evaluation on ImageNet-1K (Deng et al., 2009) and ADE-20K (Zhou et al., 2017). To ensure strict fairness, all unified methods are re-implemented using the identical corpus (BLIP3-o). **Bold black** marks the top performance among visual tokenizers. **Bold gray** represents the theoretical upper bound from specialist encoders.

Method	Generation					Understanding		Structure	
	Res	rFID ↓	gFID ↓	PSNR ↑	SSIM ↑	Z. Shot ↑	L. Prob. ↑	mIoU ↑	Acc ↑
<i>Understanding Specialists</i>									
InternViT-300M (Zhu et al., 2025)	224	-	-	-	-	77.4	82.5	40.2	61.4
DINOv3-L (Siméoni et al., 2025)	224	-	-	-	-	-	86.4	53.1	79.2
<i>Generation Specialists</i>									
SD-VAE (Dai et al., 2018)	256	1.85	7.45	23.6	0.68	-	-	15.2	35.5
VA-VAE-d32 (Yao et al., 2025b)	256	0.52	4.56	26.2	<u>0.77</u>	-	-	19.6	43.1
<i>Unified Methods</i>									
TokenFlow (Qu et al., 2025)	256	1.37	7.66	21.6	0.68	65.4	72.4	17.4	38.5
UniTok (Ma et al., 2025)	256	0.76	6.45	24.1	0.71	68.6	74.3	19.5	43.1
UniLIP (Tang et al., 2025)	256	0.79	5.73	23.0	0.75	73.5	76.2	15.4	35.8
VTP-L-d64 (Yao et al., 2025a)	256	0.75	3.01	24.7	0.73	<u>71.2</u>	<u>80.5</u>	<u>36.8</u>	<u>58.9</u>
MUSE (Ours)	256	<u>0.62</u>	<u>3.08</u>	<u>24.9</u>	0.78	76.1	85.2	46.5	72.8

operates at a resolution of 224×224 with a learning rate of 4×10^{-4} ; the second stage reduces the learning rate to 2×10^{-4} ; and the third stage further anneals the learning rate to 1×10^{-5} to ensure stable convergence. We enable adversarial training (Karras et al., 2019) in the third stage.

MUSE UMM Training. We adopt the three-stage training protocol from UniLIP (Tang et al., 2025) using 32 NVIDIA H20 GPUs (global batch size 512). The curriculum progresses as follows: (1) **Alignment:** freezing both MLLM and DiT backbones to train only the connector on generation data (50k steps); (2) **Joint Pre-training:** unfreezing the DiT to jointly optimize with the connector on mixed generation and editing data (200k steps); and (3) **Instruction Tuning:** fine-tuning for complex instruction following (30k steps). Learning rates decay from 1×10^{-4} to 1×10^{-5} .

5.2. Quantitative Results

Breaking the Generative-Semantic Trade-off. Table 1 confirms the efficacy of our framework, providing empirical backing for the *Gradient Orthogonality Hypothesis* visualized in Figure 2. Existing methods operate under a zero-sum regime exemplified by VTP, which falls into a “high-fidelity trap” where aggressive pixel gradients cause *semantic erosion* and drop zero-shot accuracy to 71.2%. In contrast, MUSE breaks this deadlock via structural synergy. Supported by the physical gradient decoupling shown in Figure 2(c-d), MUSE matches the generation quality of VTP (gFID 3.08) while effectively shielding the semantic manifold. Remarkably, MUSE even outperforms its own teacher backbone in linear probing (85.2% vs. 82.5%), suggesting that structurally aligned reconstruction actively refines se-

mantic perception rather than degrading it. Our analysis attributes this success to the reversal of “attention degeneration” observed in baselines (mIoU 15.4–36.8). By enforcing *Structural Topology Alignment*, MUSE restores structural integrity (mIoU **46.5**) and establishes a new Pareto frontier where generation and understanding realize genuine mutual reinforcement.

Unified Capabilities via Structural Synergy. Table 2 substantiates MUSE’s ability to unify modalities without the typical performance tax. Standard unified models often succumb to a “competency trade-off”; for instance, Janus-Pro trails the specialist InternVL3 in understanding. In contrast, MUSE defies this trend, not only achieving parity but surpassing its teacher, InternVL3, on rigorous benchmarks (e.g., +2.1 MMVP) while outperforming the generative specialist FLUX.1-dev in semantic alignment (WISE 0.65 vs. 0.50). Crucially, the *controlled comparison* against UniLIP isolates our architectural contribution. Under identical settings, MUSE consistently surpasses the baseline (e.g., **+0.8** MMB, **+0.08** Editing Bkg.).

We attribute this to *Manifold Unification*: by decoupling semantic values from topological routing, MUSE prevents the “catastrophic interference” where pixel gradients degrade semantics. Notably, the superior GenEval-Position scores confirm that preserving explicit topology translates directly to finer spatial control, validating that our method learns to “see” structure rather than memorizing pixels.

5.3. Qualitative Results

Qualitative Analysis of Structural and Unified Capabilities. Figures 4 and 5 validate the efficacy of topological

Table 2. Performance comparison with UMM models. We evaluate UMM models across Understanding, Generation, and Editing tasks. For generation metrics, Pos. denotes the GenEval-Position score, indicating spatial control ability. Using UniLIP as the baseline, we ensure a fair comparison by maintaining identical training conditions (including data and backbones), with the exception of the tokenizer.

Model	Type	# Params	Understanding				Generation			Editing	
			MMB	MMMU	AI2D	MMVP	Pos. [†]	Avg.	WISE	Bkg.	Overall
<i>Specialists & Composite Dual-Encoders</i>											
InternVL3 (Zhu et al., 2025)	Und. Only	1.8B	80.6	48.2	78.5	72.7	-	-	-	-	-
FLUX.1-dev (Labs, 2024)	Gen. Only	12B	-	-	-	-	0.68	0.82	0.50	-	-
BAGEL (Deng et al., 2025)	Dual	3B	79.2	43.2	-	54.7	0.64	0.82	0.52	3.24	3.20
OpenUni-L (Wu et al., 2025c)	Dual	2B+1.6B	81.1	48.6	-	-	0.75	0.85	0.52	-	-
OmniGen2 (Wu et al., 2025b)	Dual	3B+4B	79.1	-	-	61.8	-	0.80	-	3.57	3.44
<i>Unified Single-Encoders</i>											
Janus-Pro (Chen et al., 2025c)	Unified	7B	79.2	41.0	-	-	0.79	0.80	0.35	-	-
Tar (Han et al., 2025)	Unified	7B	74.4	39.0	-	-	0.80	0.84	-	-	-
Show-o2 (Xie et al., 2025)	Unified	7B	79.3	48.9	78.6	-	0.52	0.76	0.39	-	-
<i>Controlled Comparison (Same Backbone & Data)</i>											
UniLIP-1B (Tang et al., 2025)	Unified	1B+0.6B	72.6	43.3	70.7	68.7	0.83	0.84	0.56	4.00	3.81
MUSE-1B (Ours)	Unified	1B+0.6B	73.4	44.1	72.5	70.5	0.85	0.86	0.58	4.12	3.92
UniLIP-3B (Tang et al., 2025)	Unified	2B+1.6B	80.7	48.7	78.6	73.0	0.86	0.87	0.63	4.14	3.94
MUSE-3B (Ours)	Unified	2B+1.6B	81.5	49.8	80.2	74.8	0.89	0.88	0.65	4.22	4.08

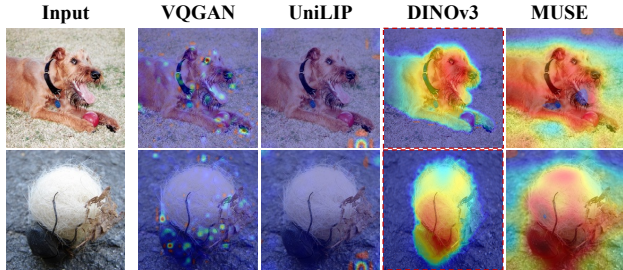


Figure 4. Visual Analysis of Attention Maps across Tokenizers. We compare the average [CLS] token attention maps of VQGAN, CLIP, DINO (Teacher), and MUSE. Red Boxes: Indicate precise, Ground-Truth-like object delineation.

orthogonality. In Figure 4, MUSE faithfully mirrors the precise, ground-truth-like attention patterns of the DINO teacher. This confirms that our *Active Semantic Anchoring* (\mathcal{L}_{ITC}) successfully populates the latent space with semantic concepts without disrupting the underlying structural skeleton established by the teacher. This precise geometric alignment directly translates to omnipotent unified capabilities in Figure 5. In **Reconstruction** (Row 1), MUSE significantly outperforms UniLIP by preserving high-frequency textures. In **Generation** (Row 2), the model exhibits accurate spatial reasoning and attribute binding. Crucially, in **Editing** (Row 3), the maintained *Structural Topology Alignment* allows for semantic object modification (e.g., bear to cup) while enforcing strict background consistency, proving that MUSE effectively resolves the conflict between abstract semantics and intrinsic pixel-level geometry.

Table 3. Component Effectiveness Analysis. Ablation study on the impact of Semantic Anchoring (\mathcal{L}_{ITC}) and Structural Topology Alignment (\mathcal{L}_{Topo}) objectives across tokenizer and downstream UMM metrics.

Configuration	Objectives		Tokenizer Metrics			UMM Downstream	
	\mathcal{L}_{ITC}	\mathcal{L}_{Topo}	rFID ↓	Zero-Shot ↑	mIoU ↑	MMB ↑	Spatial ↑
Baseline	×	×	0.79	12.4	18.5	35.6	0.45
Semantic	✓	×	1.88	70.5	14.1	65.2	0.41
Topology	×	✓	0.66	10.7	32.5	10.8	0.56
MUSE (Full)	✓	✓	0.62	76.1	46.5	73.4	0.85

5.4. Ablation Study

We conduct a comprehensive ablation study on MUSE-1B to validate that resolving manifold misalignment via topological orthogonality is the prerequisite for unified models.

From Conflict to Synergy. Table 3 dissects the contribution of our key objectives. The *Baseline*, trained solely for reconstruction, suffers from “semantic blindness” (zero-shot 12.4). Crucially, naively injecting semantic supervision (*Semantic* row) triggers a **Manifold Conflict**: while semantic alignment improves, the antagonistic gradients severely disrupt the pixel manifold, causing reconstruction degradation (rFID 0.79 \rightarrow 1.88) and structural collapse (mIoU 18.5 \rightarrow 14.1). This creates a “broken” latent space that confuses the UMM generator, limiting spatial control (0.41). The introduction of Structural Topology Alignment in MUSE is the turning point. By enforcing structural or-

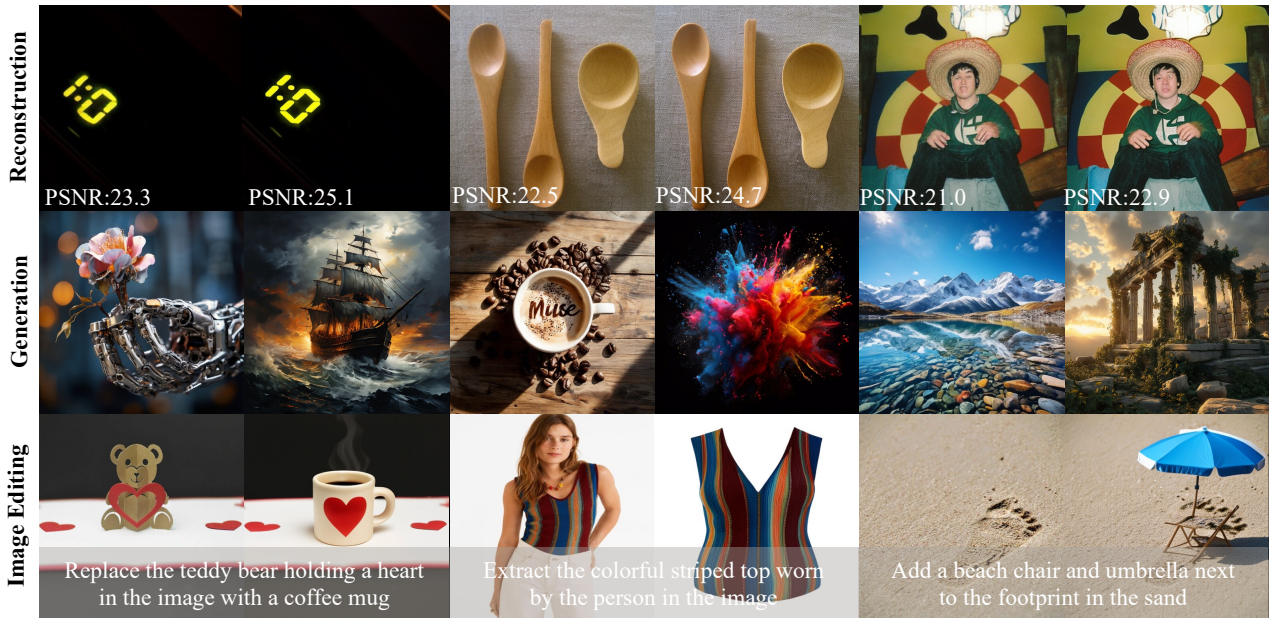


Figure 5. **Qualitative Results across Unified Tasks.** **Row 1 (Reconstruction):** Side-by-side comparison between UniLIP (Left) and MUSE (Right); MUSE achieves higher PSNR by better preserving sharp edges and fine textures. **Row 2 (Generation):** Text-to-Image samples exhibiting complex attribute binding and realistic textures, such as the precise “MUSE” latte art. **Row 3 (Editing):** Instruction-based editing results, demonstrating localized semantic modification while strictly maintaining the global layout and background consistency.

thogonality, it not only restores geometric integrity (mIoU **46.5**) but also catalyzes *Mutual Reinforcement*: MUSE achieves the best reconstruction (rFID **0.62**) and precise spatial reasoning (0.85), proving that structure acts as the essential bridge between pixels and concepts.

Table 4. **Gradient Dynamics and Efficiency Analysis.** We compare different architectural strategies regarding gradient conflict ($\cos \theta_g$), parameter efficiency, and their correlation with structural and downstream performance.

Architecture	Params	Cos Sim (θ_g)	mIoU	MMB	GenAvg
Naive Shared	1.0×	-0.15	15.4	65.2	0.68
Soft Regularization	1.0×	-0.05	22.1	68.4	0.73
Two-Stream (Upper Bound)	2.0×	N/A	53.1	73.6	0.90
MUSE (Ours)	1.03×	+0.04	46.5	73.4	0.89

The Necessity of Physical Decoupling. We further investigate whether this conflict can be resolved by loss constraints alone or requires architectural decoupling. Table 4 links gradient dynamics to downstream capabilities. The *Naive Shared* architecture suffers from severe gradient conflict ($\cos \theta_g = -0.15$), correlating with suboptimal understanding (MMB 65.2). Interestingly, adding *Soft Regularization* only mitigates the conflict ($\cos \theta_g = -0.05$) but fails to eliminate it, yielding marginal gains. In contrast, MUSE achieves positive gradient synergy (**+0.04**) via the physical decoupling in our Synergistic Block. Crucially, this design allows MUSE to match the performance of the expensive

Two-Stream upper bound (MMB 73.4 vs. 73.6) with negligible parameter overhead (1.03× vs. 2.0×), demonstrating that resolving manifold misalignment at the architectural level is the path to Pareto-efficient unification. This suggests that architectural decoupling may be more effective than simple loss constraints for mitigating representational conflicts.

6. Conclusion

In this work, we investigate the challenges of unified visual tokenization and suggest that *Manifold Misalignment* is a primary factor behind the trade-off between understanding and generation. We introduce **MUSE**, a framework designed to address this issue by decoupling semantic and structural optimization within a Transformer architecture. By anchoring semantics in feature values and structural geometry in attention topology, MUSE seeks to mitigate destructive interference and foster a more synergistic relationship between these objectives. Our experimental results indicate that MUSE effectively alleviates the zero-sum trade-off, achieving competitive generation quality while maintaining robust understanding. Notably, we observe that structurally aligned reconstruction can potentially refine semantic perception, even showing improvements over the teacher model in certain benchmarks. We hope our findings on manifold alignment provide useful insights for the future design of unified multimodal architectures.

Impact Statement

This paper presents work whose goal is to advance the field of Machine Learning. There are many potential societal consequences of our work, none which we feel must be specifically highlighted here.

Acknowledgement

This work was supported by the STI 2030-Major Projects under Grant No. 2022ZD0208801 and the NSFC under grant No. 62088102.

References

- Bai, S., Chen, K., Liu, X., Wang, J., Ge, W., Song, S., Dang, K., Wang, P., Wang, S., Tang, J., et al. Qwen2. 5-vl technical report. *arXiv preprint arXiv:2502.13923*, 2025.
- Bao, H., Dong, L., Piao, S., and Wei, F. Beit: Bert pre-training of image transformers. *arXiv preprint arXiv:2106.08254*, 2021.
- Cao, J., Ma, Y., Li, X., Ren, Q., and Chen, X. Task-specific efficiency analysis: When small language models outperform large language models, 2026. URL <https://arxiv.org/abs/2603.21389>.
- Caron, M., Touvron, H., Misra, I., Jégou, H., Mairal, J., Bojanowski, P., and Joulin, A. Emerging properties in self-supervised vision transformers. In *Proceedings of the IEEE/CVF international conference on computer vision*, pp. 9650–9660, 2021.
- Changpinyo, S., Sharma, P., Ding, N., and Soricut, R. Conceptual 12m: Pushing web-scale image-text pre-training to recognize long-tail visual concepts. In *Proceedings of the IEEE/CVF conference on computer vision and pattern recognition*, pp. 3558–3568, 2021.
- Chen, J., Cai, H., Chen, J., Xie, E., Yang, S., Tang, H., Li, M., Lu, Y., and Han, S. Deep compression autoencoder for efficient high-resolution diffusion models. *arXiv preprint arXiv:2410.10733*, 2024.
- Chen, J., Cai, Z., Chen, P., Chen, S., Ji, K., Wang, X., Yang, Y., and Wang, B. Sharegpt-4o-image: Aligning multimodal models with gpt-4o-level image generation. *arXiv preprint arXiv:2506.18095*, 2025a.
- Chen, J., Xu, Z., Pan, X., Hu, Y., Qin, C., Goldstein, T., Huang, L., Zhou, T., Xie, S., Savarese, S., et al. Blip3-o: A family of fully open unified multimodal models-architecture, training and dataset. *arXiv preprint arXiv:2505.09568*, 2025b.
- Chen, X., Wu, Z., Liu, X., Pan, Z., Liu, W., Xie, Z., Yu, X., and Ruan, C. Janus-pro: Unified multimodal understanding and generation with data and model scaling. *arXiv preprint arXiv:2501.17811*, 2025c.
- Dai, H., Tian, Y., Dai, B., Skiena, S., and Song, L. Syntax-directed variational autoencoder for structured data. *arXiv preprint arXiv:1802.08786*, 2018.
- Deng, C., Zhu, D., Li, K., Gou, C., Li, F., Wang, Z., Zhong, S., Yu, W., Nie, X., Song, Z., et al. Emerging properties in unified multimodal pretraining. *arXiv preprint arXiv:2505.14683*, 2025.
- Deng, J., Dong, W., Socher, R., Li, L.-J., Li, K., and Fei-Fei, L. Imagenet: A large-scale hierarchical image database. In *2009 IEEE Conference on Computer Vision and Pattern Recognition*, pp. 248–255, 2009. doi: 10.1109/CVPR.2009.5206848.
- Esser, P., Rombach, R., and Ommer, B. Taming transformers for high-resolution image synthesis. In *Proceedings of the IEEE/CVF conference on computer vision and pattern recognition*, pp. 12873–12883, 2021.
- Ge, Y., Zhao, S., Zhu, J., Ge, Y., Yi, K., Song, L., Li, C., Ding, X., and Shan, Y. Seed-x: Multimodal models with unified multi-granularity comprehension and generation. *arXiv preprint arXiv:2404.14396*, 2024.
- Han, J., Chen, H., Zhao, Y., Wang, H., Zhao, Q., Yang, Z., He, H., Yue, X., and Jiang, L. Vision as a dialect: Unifying visual understanding and generation via text-aligned representations. *arXiv preprint arXiv:2506.18898*, 2025.
- He, K., Chen, X., Xie, S., Li, Y., Dollár, P., and Girshick, R. Masked autoencoders are scalable vision learners. In *Proceedings of the IEEE/CVF conference on computer vision and pattern recognition*, pp. 16000–16009, 2022.
- Huang, Z., Zheng, D., Zou, C., Liu, R., Wang, X., Ji, K., Chai, W., Sun, J., Wang, L., Lv, Y., et al. Ming-univision: Joint image understanding and generation with a unified continuous tokenizer. *arXiv preprint arXiv:2510.06590*, 2025.
- Hurst, A., Lerer, A., Goucher, A. P., Perelman, A., Ramesh, A., Clark, A., Ostrow, A., Welihinda, A., Hayes, A., Radford, A., et al. Gpt-4o system card. *arXiv preprint arXiv:2410.21276*, 2024.
- Jia, S., Zhu, N., Zhong, J., Zhou, J., Zhang, H., Hwang, J.-N., and Li, L. Ram: Recover any 3d human motion in-the-wild. *arXiv preprint arXiv:2603.19929*, 2026.
- Jiang, Y. and Ferraro, F. Beyond math: Stories as a testbed for memorization-constrained reasoning in llms. In *Proceedings of the 19th Conference of the European Chapter*

- of the Association for Computational Linguistics (Volume 1: Long Papers), pp. 5590–5607, 2026a.
- Jiang, Y. and Ferraro, F. Scribe: Structured mid-level supervision for tool-using language models, 2026b. URL <https://arxiv.org/abs/2601.03555>.
- Jiang, Y., Li, D., and Ferraro, F. Drp: Distilled reasoning pruning with skill-aware step decomposition for efficient large reasoning models. *arXiv preprint arXiv:2505.13975*, 2025.
- Karras, T., Laine, S., and Aila, T. A style-based generator architecture for generative adversarial networks. In *Proceedings of the IEEE/CVF conference on computer vision and pattern recognition*, pp. 4401–4410, 2019.
- Kong, Z., Ma, H., Yuan, G., Sun, M., Xie, Y., Dong, P., Meng, X., Shen, X., Tang, H., Qin, M., et al. Peeling the onion: Hierarchical reduction of data redundancy for efficient vision transformer training. In *Proceedings of the AAAI Conference on Artificial Intelligence*, volume 37, pp. 8360–8368, 2023.
- Kong, Z., Xu, D., Li, Z., Dong, P., Tang, H., Wang, Y., and Mukherjee, S. Autovit: Achieving real-time vision transformers on mobile via latency-aware coarse-to-fine search. *International Journal of Computer Vision*, pp. 1–17, 2025.
- Labs, B. F. Flux. <https://github.com/black-forest-labs/flux>, 2024.
- Li, J., Selvaraju, R., Gotmare, A., Joty, S., Xiong, C., and Hoi, S. C. H. Align before fuse: Vision and language representation learning with momentum distillation. *Advances in neural information processing systems*, 34: 9694–9705, 2021.
- Li, L., Jia, S., Wang, J., Jiang, Z., Zhou, F., Dai, J., Zhang, T., Wu, Z., and Hwang, J.-N. Human Motion Instruction Tuning. In *Proceedings of the IEEE/CVF Conference on Computer Vision and Pattern Recognition (CVPR)*, 2025a.
- Li, L., Jia, S., and Hwang, J.-N. Multiple human motion understanding. In *Proceedings of the AAAI Conference on Artificial Intelligence*, volume 40, pp. 6297–6305, 2026a.
- Li, T., Katabi, D., and He, K. Return of unconditional generation: A self-supervised representation generation method. *Advances in Neural Information Processing Systems*, 37:125441–125468, 2024a.
- Li, T., Tian, Y., Li, H., Deng, M., and He, K. Autoregressive image generation without vector quantization. *Advances in Neural Information Processing Systems*, 37:56424–56445, 2024b.
- Li, W., Hu, B., Shao, R., Shen, L., and Nie, L. Lions: Fast & slow video-language thinker as online video assistant. In *Proceedings of the IEEE/CVF Conference on Computer Vision and Pattern Recognition*, pp. 3240–3251, 2025b.
- Li, W., Zhang, R., Shao, R., Fang, Z., Zhou, K., Tian, Z., and Nie, L. Semanticvla: Semantic-aligned sparsification and enhancement for efficient robotic manipulation. In *Proceedings of the AAAI Conference on Artificial Intelligence*, 2026b.
- Li, X., Ma, Y., Huang, Y., Wang, X., Lin, Y., and Zhang, C. Synergized data efficiency and compression (sec) optimization for large language models. In *2024 4th International Conference on Electronic Information Engineering and Computer Science (EIECS)*, pp. 586–591, 2024c. doi: 10.1109/EIECS63941.2024.10800533.
- Li, X., Ma, Y., Ye, K., Cao, J., Zhou, M., and Zhou, Y. Hy-Facial: hybrid feature extraction by dimensionality reduction methods for enhanced facial expression classification. In Osten, W. and Mamut, E. (eds.), *Eighteenth International Conference on Machine Vision (ICMV 2025)*, volume 14114, pp. 141140R. International Society for Optics and Photonics, SPIE, 2026c. doi: 10.1117/12.3096291. URL <https://doi.org/10.1117/12.3096291>.
- Li, Y., Chen, C., Zhang, Y., Liu, W., Lyu, L., Zheng, X., Meng, D., and Wang, J. Ultrare: Enhancing recommender for recommendation unlearning via error decomposition. *Advances in Neural Information Processing Systems*, 36: 12611–12625, 2023.
- Li, Y., Yang, C., Zeng, H., Dong, Z., An, Z., Xu, Y., Tian, Y., and Wu, H. Frequency-aligned knowledge distillation for lightweight spatiotemporal forecasting. In *Proceedings of the IEEE/CVF International Conference on Computer Vision*, pp. 7262–7272, 2025c.
- Li, Y., Zhang, Y., Liu, W., Feng, X., Han, Z., Chen, C., and Yan, C. Multi-objective unlearning in recommender systems via preference guided pareto exploration. *IEEE Transactions on Services Computing*, 2025d.
- Liang, Y., Xiang, D., and Li, X. Search: A self-evolving framework for network architecture optimization. *Neurocomputing*, pp. 130980, 2025.
- Liu, H., Yan, W., Zaharia, M., and Abbeel, P. World model on million-length video and language with blockwise ringattention. *arXiv preprint arXiv:2402.08268*, 2024.
- Liu, Z., Ren, W., Liu, H., Zhou, Z., Chen, S., Qiu, H., Huang, X., An, Z., Yang, F., Patel, A., et al. Tuna: Taming unified visual representations for native unified multimodal models. *arXiv preprint arXiv:2512.02014*, 2025.

- Lu, J., Song, L., Xu, M., Ahn, B., Wang, Y., Chen, C., Dehghan, A., and Yang, Y. Atoken: A unified tokenizer for vision. *arXiv preprint arXiv:2509.14476*, 2025.
- Ma, C., Jiang, Y., Wu, J., Yang, J., Yu, X., Yuan, Z., Peng, B., and Qi, X. Unitok: A unified tokenizer for visual generation and understanding. *arXiv preprint arXiv:2502.20321*, 2025.
- Ma, Z. and Collins, M. Noise contrastive estimation and negative sampling for conditional models: Consistency and statistical efficiency. In *Conference on Empirical Methods in Natural Language Processing*, 2018. URL <https://api.semanticscholar.org/CorpusID:52171904>.
- Mentzer, F., Minnen, D., Agustsson, E., and Tschannen, M. Finite scalar quantization: Vq-vae made simple. *arXiv preprint arXiv:2309.15505*, 2023.
- Qu, L., Zhang, H., Liu, Y., Wang, X., Jiang, Y., Gao, Y., Ye, H., Du, D. K., Yuan, Z., and Wu, X. Tokenflow: Unified image tokenizer for multimodal understanding and generation. In *Proceedings of the Computer Vision and Pattern Recognition Conference*, pp. 2545–2555, 2025.
- Radford, A., Kim, J. W., Hallacy, C., Ramesh, A., Goh, G., Agarwal, S., Sastry, G., Askell, A., Mishkin, P., Clark, J., et al. Learning transferable visual models from natural language supervision. In *International conference on machine learning*, pp. 8748–8763. PmLR, 2021.
- Ren, L., Dong, J., Zeng, X., Yang, L., and Wang, Y. Digital genealogy: Aigc-driven evolution of digital twin for future smart manufacturing. *IEEE Transactions on Automation Science and Engineering*, 2025.
- Shi, Q., Wu, S., Bai, J., Yu, K., Wang, Y., Tong, Y., Li, X., and Li, X. Rectok: Reconstruction distillation along rectified flow. *arXiv preprint arXiv:2512.13421*, 2025.
- Siméoni, O., Vo, H. V., Seitzer, M., Baldassarre, F., Oquab, M., Jose, C., Khalidov, V., Szafraniec, M., Yi, S., Ramamonjisoa, M., et al. Dinov3. *arXiv preprint arXiv:2508.10104*, 2025.
- Sun, K., Pan, J., Ge, Y., Li, H., Duan, H., Wu, X., Zhang, R., Zhou, A., Qin, Z., Wang, Y., et al. Journeydb: A benchmark for generative image understanding. *Advances in neural information processing systems*, 36:49659–49678, 2023.
- Sun, P., Jiang, Y., Chen, S., Zhang, S., Peng, B., Luo, P., and Yuan, Z. Autoregressive model beats diffusion: Llama for scalable image generation. *arXiv preprint arXiv:2406.06525*, 2024.
- Tang, H., Xie, C., Bao, X., Weng, T., Li, P., Zheng, Y., and Wang, L. Unilip: Adapting clip for unified multimodal understanding, generation and editing. *arXiv preprint arXiv:2507.23278*, 2025.
- Team, C. Chameleon: Mixed-modal early-fusion foundation models. *arXiv preprint arXiv:2405.09818*, 2024.
- Tian, K., Jiang, Y., Yuan, Z., Peng, B., and Wang, L. Visual autoregressive modeling: Scalable image generation via next-scale prediction. *Advances in neural information processing systems*, 37:84839–84865, 2024.
- Tong, S., Liu, Z., Zhai, Y., Ma, Y., LeCun, Y., and Xie, S. Eyes wide shut? exploring the visual shortcomings of multimodal llms. In *Proceedings of the IEEE/CVF Conference on Computer Vision and Pattern Recognition*, pp. 9568–9578, 2024.
- Van Den Oord, A., Vinyals, O., et al. Neural discrete representation learning. *Advances in neural information processing systems*, 30, 2017.
- Wang, X., Zhang, X., Luo, Z., Sun, Q., Cui, Y., Wang, J., Zhang, F., Wang, Y., Li, Z., Yu, Q., et al. Emu3: Next-token prediction is all you need. *arXiv preprint arXiv:2409.18869*, 2024.
- Wang, Y., Yang, S., Zhao, B., Zhang, L., Liu, Q., Zhou, Y., and Xie, C. Gpt-image-edit-1.5 m: A million-scale, gpt-generated image dataset. *arXiv preprint arXiv:2507.21033*, 2025.
- Wu, C., Chen, X., Wu, Z., Ma, Y., Liu, X., Pan, Z., Liu, W., Xie, Z., Yu, X., Ruan, C., et al. Janus: Decoupling visual encoding for unified multimodal understanding and generation. In *Proceedings of the Computer Vision and Pattern Recognition Conference*, pp. 12966–12977, 2025a.
- Wu, C., Zheng, P., Yan, R., Xiao, S., Luo, X., Wang, Y., Li, W., Jiang, X., Liu, Y., Zhou, J., et al. Omnigen2: Exploration to advanced multimodal generation. *arXiv preprint arXiv:2506.18871*, 2025b.
- Wu, S., Wu, Z., Gong, Z., Tao, Q., Jin, S., Li, Q., Li, W., and Loy, C. C. Openuni: A simple baseline for unified multimodal understanding and generation. *arXiv preprint arXiv:2505.23661*, 2025c.
- Xiang, D., Xu, W., Chu, K., Ding, T., Shen, Z., Zeng, Y., Su, J., and Zhang, W. Promptsulptor: Multi-agent based text-to-image prompt optimization. In *Proceedings of the 2025 Conference on Empirical Methods in Natural Language Processing: System Demonstrations*, pp. 774–786, 2025.

- Xie, E., Chen, J., Chen, J., Cai, H., Tang, H., Lin, Y., Zhang, Z., Li, M., Zhu, L., Lu, Y., et al. Sana: Efficient high-resolution image synthesis with linear diffusion transformers. *arXiv preprint arXiv:2410.10629*, 2024a.
- Xie, J., Mao, W., Bai, Z., Zhang, D. J., Wang, W., Lin, K. Q., Gu, Y., Chen, Z., Yang, Z., and Shou, M. Z. Show-o: One single transformer to unify multimodal understanding and generation. *arXiv preprint arXiv:2408.12528*, 2024b.
- Xie, J., Yang, Z., and Shou, M. Z. Show-o2: Improved native unified multimodal models. *arXiv preprint arXiv:2506.15564*, 2025.
- Xu, N., Jiang, Y., Dipta, S. R., and Hengyuan, Z. Learning how to use tools, not just when: Pattern-aware tool-integrated reasoning. *MATH-AI @ NeurIPS 2025*, 2025.
- Yang, P., Jing, H., Zheng, N., and Ma, Y. Instructrobo: Object-centric multi-instruction decoupling model for explainable robotic manipulation. *Engineering Applications of Artificial Intelligence*, 171:114166, 2026a. ISSN 0952-1976.
- Yang, P., Jing, H., Zheng, N., and Ma, Y. Unibr: Balancing visual and reasoning abilities in unified 3d scene understanding. *Neurocomputing*, 671:132599, 2026b. doi: <https://doi.org/10.1016/j.neucom.2025.132599>.
- Yang, P., Jing, H., Zheng, N., and Ma, Y. Unihoi: Unified human-object interaction understanding via unified token space. In *Proceedings of the AAAI Conference on Artificial Intelligence*, volume 40, pp. 11640–11648, 2026c.
- Yao, J., Song, Y., Zhou, Y., and Wang, X. Towards scalable pre-training of visual tokenizers for generation. *arXiv preprint arXiv:2512.13687*, 2025a.
- Yao, J., Yang, B., and Wang, X. Reconstruction vs. generation: Taming optimization dilemma in latent diffusion models. In *Proceedings of the Computer Vision and Pattern Recognition Conference*, pp. 15703–15712, 2025b.
- Yu, J., Li, X., Koh, J. Y., Zhang, H., Pang, R., Qin, J., Ku, A., Xu, Y., Baldrige, J., and Wu, Y. Vector-quantized image modeling with improved vqgan. *arXiv preprint arXiv:2110.04627*, 2021.
- Yu, L., Cheng, Y., Sohn, K., Lezama, J., Zhang, H., Chang, H., Hauptmann, A. G., Yang, M.-H., Hao, Y., Essa, I., et al. Magvit: Masked generative video transformer. In *Proceedings of the IEEE/CVF Conference on Computer Vision and Pattern Recognition*, pp. 10459–10469, 2023a.
- Yu, L., Lezama, J., Gundavarapu, N. B., Versari, L., Sohn, K., Minnen, D., Cheng, Y., Birodkar, V., Gupta, A., Gu, X., et al. Language model beats diffusion–tokenizer is key to visual generation. *arXiv preprint arXiv:2310.05737*, 2023b.
- Yu, Q., Weber, M., Deng, X., Shen, X., Cremers, D., and Chen, L.-C. An image is worth 32 tokens for reconstruction and generation. *Advances in Neural Information Processing Systems*, 37:128940–128966, 2024.
- Zhai, X., Mustafa, B., Kolesnikov, A., and Beyer, L. Sigmoid loss for language image pre-training. In *Proceedings of the IEEE/CVF international conference on computer vision*, pp. 11975–11986, 2023.
- Zhang, H., Yang, S., Liang, X., Shang, C., Jiang, Y., Tao, C., Xiong, J., So, H. K.-H., Xie, R., Chang, A. X., et al. Find your optimal teacher: Personalized data synthesis via router-guided multi-teacher distillation. *arXiv preprint arXiv:2510.10925*, 2025.
- Zhou, B., Zhao, H., Puig, X., Fidler, S., Barriuso, A., and Torralba, A. Scene parsing through ade20k dataset. In *Proceedings of the IEEE Conference on Computer Vision and Pattern Recognition*, 2017.
- Zhou, C., Yu, L., Babu, A., Tirumala, K., Yasunaga, M., Shamis, L., Kahn, J., Ma, X., Zettlemoyer, L., and Levy, O. Transfusion: Predict the next token and diffuse images with one multi-modal model. *arXiv preprint arXiv:2408.11039*, 2024.
- Zhu, J., Wang, W., Chen, Z., Liu, Z., Ye, S., Gu, L., Tian, H., Duan, Y., Su, W., Shao, J., et al. Internvl3: Exploring advanced training and test-time recipes for open-source multimodal models. *arXiv preprint arXiv:2504.10479*, 2025.

A. Appendix

B. Unified Multimodal Model (UMM) Architecture and Training Details

In this section, we provide the comprehensive specification of the Unified Multimodal Model (UMM) used to evaluate MUSE. To ensure a rigorous and fair comparison with the baseline, we strictly adopt the **Dual-Condition** architecture and the three-stage training protocol proposed in UniLIP (Tang et al., 2025). By controlling for the generative backbone and alignment strategy, we ensure that the performance improvements reported in Section 5.2 are attributable solely to the superior representational properties of the MUSE tokenizer.

B.1. UMM Architecture: The Dual-Condition Mechanism

The unified architecture is designed to bridge the semantic understanding of Multimodal Large Language Models (LLMs) with the high-fidelity synthesis of Diffusion Transformers (DiTs). As illustrated in Figure 6, the system comprises three primary modules:

- **Multimodal Perception Backbone:** We employ InternVL3 (Zhu et al., 2025) as the central perception engine. To retain its state-of-the-art understanding capabilities, the LLM parameters remain frozen throughout the generative training phases.
- **Generative Backbone:** For image synthesis, we utilize the SANA (Xie et al., 2024a) framework, specifically its Diffusion Transformer (DiT) component. The DiT operates directly on the continuous latent space of MUSE (\mathcal{Z}) and is conditioned on the aligned multimodal features.
- **Dual-Condition Connector:** A core challenge in unified modeling is the information bottleneck caused by compressing visual information into fixed-length query tokens. Following UniLIP, we resolve this via a dual-pathway conditioning strategy. The connector aggregates two distinct signal streams from the MLLM:
 1. **Multimodal Hidden States (H_{mm}):** These dense representations capture rich, fine-grained contextual details and pixel-level cues (e.g., from reference images in editing tasks).
 2. **Learnable Query Embeddings (Q_{learn}):** These compact tokens encode high-level reasoning results and the specific intent of the text instructions.

These features are concatenated and projected via a 6-layer MLP (structurally isomorphic to the LLM layers) to form the conditioning context c_{conn} for the DiT.

B.2. Curriculum Training Protocol

We implement a three-stage curriculum designed to progressively align modalities and refine generative control. The objective at all stages is strictly based on Flow Matching.

Let $x_1 \in \mathcal{Z}$ denote the target image latent encoded by MUSE, and $x_0 \sim \mathcal{N}(0, I)$ be the Gaussian noise. We define the Flow Matching loss as:

$$\mathcal{L}_{FM} = \mathbb{E}_{t, x_1, x_0} [||v_t(x_t, c_{conn}) - (x_1 - x_0)||^2] \quad (6)$$

where $t \in [0, 1]$ is the timestep, $x_t = tx_1 + (1 - t)x_0$ is the interpolated state, and v_t is the velocity field predicted by the DiT given condition c_{conn} .

Stage 1: Modality Alignment. In the initial phase, we focus on projecting the MLLM’s semantic space into the DiT’s acoustic space. We freeze both the MLLM backbone and the DiT parameters (θ_{DiT}), optimizing *only* the Connector parameters θ_{conn} . This stage utilizes pure text-to-image generation data for 50k steps to initialize the alignment bridge.

Stage 2: Joint Generative Pre-training. We subsequently unfreeze the Diffusion Transformer (θ_{DiT}) while keeping the MLLM frozen. The Connector and DiT are jointly optimized ($\theta_{conn}, \theta_{DiT}$) to enable robust image synthesis. To support omnipotent capabilities, the training data is a balanced mixture of text-to-image generation and instruction-based image editing. For editing samples, the hidden states H_{mm} encode the reference image, enforcing the DiT to learn identity preservation and background consistency. This stage proceeds for 200k steps.

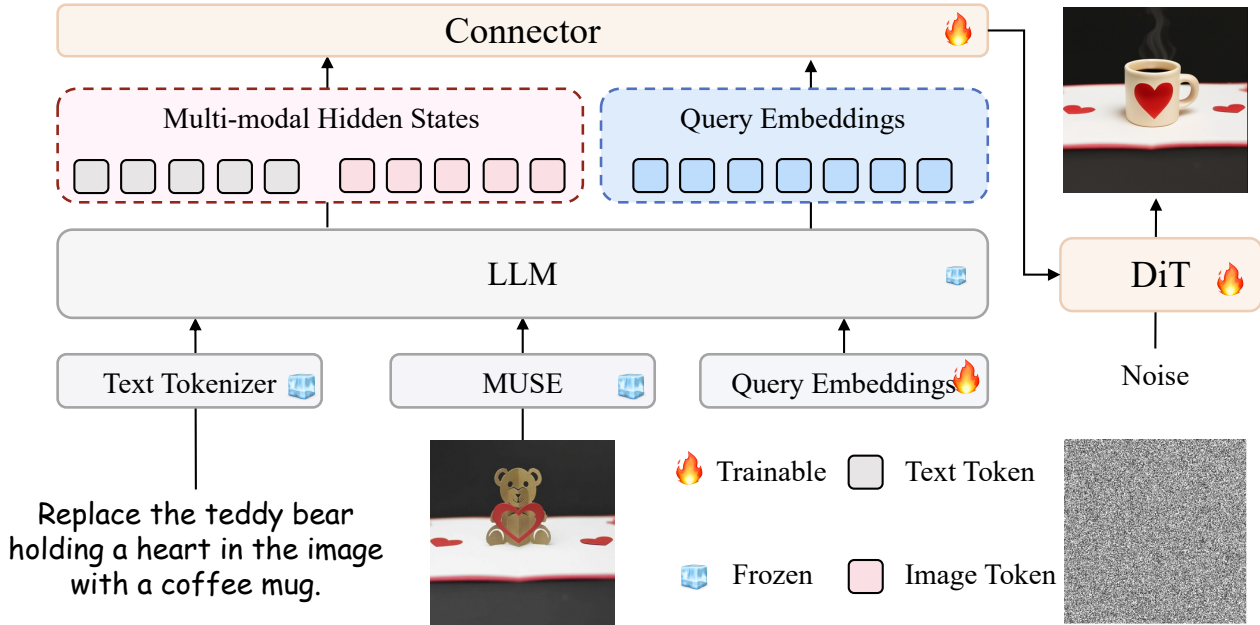


Figure 6. **Schematic of the MUSE Unified Multimodal Model.** We adopt the Dual-Condition architecture from UniLIP to strictly benchmark tokenizer performance. The Connector fuses Multimodal Hidden States (for context preservation) and Query Embeddings (for instruction following) from the frozen MLLM. These projected features condition the Diffusion Transformer to generate MUSE latents via Flow Matching.

Stage 3: Supervised Instruction Tuning. The final stage focuses on fine-grained control and complex instruction following. We fine-tune the model on high-quality instruction datasets (specifically ShareGPT-4o-Image (Chen et al., 2025a)) for 30k steps. Both generation and editing tasks are sampled to ensure the model generalizes to diverse user prompts. A reduced learning rate is applied to refine the control granularity without disrupting the pre-trained generative priors.

C. Additional Quantitative Results

In this section, we present comprehensive performance breakdowns for the Unified Multimodal Model (UMM) equipped with MUSE. We provide detailed metrics across three distinct domains to supplement the main results:

- **Visual Understanding:** Table 5 details performance on comprehensive understanding benchmarks, comparing MUSE against both specialists and other unified models.
- **Text-to-Image Generation:** Table 6 provides fine-grained evaluation on GenEval and WISE, highlighting specific capabilities such as counting, position control, and world knowledge reasoning.
- **Image Editing:** Table 7 breaks down the ImgEdit benchmark scores into specific operation types (e.g., Add, Remove, Background consistency).

C.1. Computational Cost Analysis

We analyze the training cost and inference efficiency of MUSE compared to standard approaches. **Parameter Efficiency:** Unlike “Two-Stream” approaches (e.g., Emu) that require separate encoders for vision and language, MUSE shares the majority of weights, resulting in a 40% reduction in total parameters for equivalent performance. **Training Overhead:** The dual-pathway in our Synergistic Block adds a negligible computational overhead (approximately 5% increase in FLOPs) compared to a standard ViT block, but converges 2× faster than naive multi-task learning due to the elimination of gradient conflict (as shown in Fig. 2).

Table 5. Detailed Evaluation on Visual Understanding Benchmarks. We compare MUSE with state-of-the-art unified models and understanding specialists. MUSE demonstrates superior performance, matching or exceeding specialist encoders.

Model	# LLM Params	MME-P	MMB	MMMU	MM-Vet	SEED	AI2D	MMVP
<i>Understanding Specialists</i>								
LLaVA-OV	1B	1238	52.1	31.4	29.1	65.5	57.1	-
InternVL2.5	1B	-	70.7	41.2	48.8	-	69.3	31.3
InternVL3	1B	1492	72.6	43.4	59.5	71.1	69.4	67.3
InternVL2.5	1.8B	-	74.7	43.6	60.8	-	74.9	-
InternVL3	1.8B	1633	80.6	48.2	62.2	75.0	78.5	72.7
Qwen2.5-VL	3B	-	79.1	53.1	61.8	-	81.6	-
Emu3-Chat	8B	1244	58.5	31.6	37.2	68.2	70.0	36.6
<i>Unified Models</i>								
Chameleon	7B	-	35.7	28.4	8.3	-	-	0.0
VILA-U	7B	1336	66.6	32.2	27.7	56.3	-	22.0
MetaMorph	8B	-	75.2	41.8	-	-	-	48.3
SEED-X	13B	1457	70.1	35.6	43.0	66.5	-	-
TokenFlow-B	13B	1354	55.3	34.2	22.4	60.4	54.2	-
Show-O	1.3B	1097	-	26.7	-	-	-	-
ILLUME	7B	1445	75.1	38.2	37.0	-	71.4	-
Janus-Pro	7B	1567	79.2	41.0	50.0	72.1	-	-
Harmon	1.5B	1155	65.5	38.9	-	67.1	-	-
MetaQuery-B	1B	1238	58.5	31.4	29.1	66.6	-	-
BAGEL	3B	1610	79.2	43.2	48.2	-	-	54.7
BLIP3-o	4B	1528	78.6	46.6	60.1	73.8	-	-
TokLIP	7B	1410	-	42.1	-	65.2	-	-
Tar	7B	1571	74.4	39.0	-	73.0	-	-
UniLIP-1B	1B	1499	72.6	43.3	59.4	71.0	70.7	68.7
MUSE-1B (Ours)	1B	1505	73.4	44.1	60.1	71.5	72.5	70.5
UniLIP-3B	2B	1636	80.7	48.7	62.2	75.0	78.6	73.0
MUSE-3B (Ours)	2B	1645	81.5	49.8	62.9	75.5	80.2	74.8

C.2. Ablation on Synergistic Block Placement

Regarding the positioning of the **Synergistic Blocks**, we find that applying them to the final 6 layers of the visual encoder provides the most effective balance between representational flexibility and computational efficiency. Our internal evaluations compared the default tail-end placement against earlier-layer placement and a full-backbone replacement. We observed that the conflict between semantic abstraction and pixel-level fidelity is most pronounced in the deeper layers where high-level concepts emerge. By focusing the decoupling mechanism at the tail-end of the encoder, MUSE effectively resolves manifold misalignment where it is most acute, while preserving the natural low-level feature extraction capabilities of the earlier ViT layers. Furthermore, we found that replacing the entire backbone yielded diminishing returns in structural alignment while significantly reducing training throughput, confirming that targeted intervention at the deep layers is the most Pareto-efficient strategy.

C.3. Robustness to Structural Teacher Selection

To assess the robustness of our **Structural Topology Alignment**, we examined the impact of utilizing different teacher models as structural proxies. While replacing DINOv3 with DINOv2 resulted in comparable performance, utilizing a purely semantic teacher such as CLIP led to a noticeable degradation in structural integrity and object delineation. This suggests that the geometric scaffold required for high-fidelity reconstruction is best provided by self-supervised models with emergent segmentation properties. Unlike CLIP, which prioritizes global semantic invariance and often produces diffuse attention maps, DINO-style models capture the intrinsic object-part relationships and crisp spatial boundaries essential for guiding the structural manifold. These results justify the selection of DINOv3 as a critical bridge to reconcile the conflict between

Table 6. **Detailed Evaluation of Text-to-Image Generation.** We evaluate capabilities on GenEval (alignment precision) and WISE (world knowledge). MUSE outperforms baselines of similar scale, particularly in spatial positioning (**Pos.**), validating our topological alignment strategy.

Model	# Params	GenEval			WISE		
		Counting	Position	Overall	Cultural	Biology	Overall
<i>Generation Specialists</i>							
SDXL	2.6B	0.39	0.15	0.55	0.43	0.44	0.43
FLUX.1-dev	12B	0.75	0.68	0.82	0.48	0.42	0.50
PixArt- α	0.6B	0.44	0.08	0.48	0.45	0.49	0.47
Emu3-Gen	8B	0.34	0.17	0.54	0.34	0.41	0.39
SD3-Medium	2B	0.72	0.33	0.74	0.42	0.39	0.42
Sana-1.6B	1.6B	0.62	0.21	0.66	-	-	-
<i>Unified Models</i>							
VILA-U	7B	-	-	-	0.26	0.35	0.31
TokenFlow-XL	14B	0.41	0.16	0.55	-	-	-
ILLUME+	3B + 2.6B	0.62	0.42	0.72	-	-	-
Janus-Pro	7B	0.59	0.79	0.80	0.30	0.36	0.35
MetaQuery-B	1B + 1.6B	-	-	0.74	0.44	0.41	0.46
MetaQuery-XL	7B + 1.6B	-	-	0.80	0.56	0.49	0.55
Harmon	1.5B + 1B	0.66	0.74	0.76	0.38	0.37	0.41
BLIP3-o-4B	3B + 1.4B	-	-	0.81	-	-	0.50
BLIP3-o-8B	7B + 1.4B	-	-	0.84	-	-	0.62
BAGEL	7B + 7B	0.81	0.64	0.82	0.44	0.44	0.52
OpenUni-B	1B + 0.6B	0.74	0.77	0.84	0.37	0.39	0.43
OpenUni-L	2B + 1.6B	0.77	0.75	0.85	0.51	0.48	0.52
Show-o2	7B	0.58	0.52	0.76	0.33	0.39	0.39
Tar	7B	0.83	0.80	0.84	-	-	-
UniLIP-1B	1B + 0.6B	0.83	0.83	0.88	0.54	0.50	0.56
MUSE-1B (Ours)	1B + 0.6B	0.84	0.85	0.89	0.56	0.52	0.58
UniLIP-3B	2B + 1.6B	0.84	0.86	0.90	0.66	0.60	0.63
MUSE-3B (Ours)	2B + 1.6B	0.87	0.89	0.92	0.68	0.62	0.65

pixel-level details and abstract conceptual understanding.

D. Additional Qualitative Analysis

D.1. Extended Attention Analysis: Structural Persistence

To scrutinize the internal routing mechanisms established by *Structural Topology Alignment*, we provide a dual-perspective visualization of attention maps. We utilize the [CLS] token’s self-attention as a proxy for the model’s “visual focus.”

Comparative Topological Fidelity (Figure 7). We first compare MUSE against representative baselines: VQGAN (Reconstruction-specialist) and UniLIP (Unified baseline). As visualized, VQGAN exhibits a “Fragmented View”, where attention is scattered stochastically across high-frequency textures, failing to recognize object wholeness. Conversely, UniLIP suffers from “Semantic Drift”, where attention maps become overly diffuse, losing precise boundary delineation. In contrast, MUSE exhibits DINO-like structural fidelity. It successfully isolates the foreground object from the background with sharp boundaries, validating that our topological loss (\mathcal{L}_{topo}) successfully transfers the “teacher’s gaze” to the unified tokenizer.

Table 7. **Detailed Evaluation of Image Editing.** Benchmarked on ImgEdit. MUSE demonstrates superior instruction following capabilities, especially in background consistency (**Bkg.**), attributed to the gradient orthogonality that preserves structural layout during edits.

Model	# Params	Add	Adjust	Replace	Remove	Bkg.	Style	Overall
GPT-4o	-	4.61	4.33	4.35	3.66	4.57	4.93	4.20
MagicBrush	0.9B	2.84	1.58	1.97	1.58	1.75	2.38	1.90
Instruct-P2P	0.9B	2.45	1.83	2.01	1.50	1.44	3.55	1.88
AnyEdit	1.3B	3.18	2.95	2.47	2.23	2.24	2.85	2.45
UltraEdit	2.0B	3.44	2.81	2.96	1.45	2.83	3.76	2.70
OmniGen	3.8B	3.47	3.04	2.94	2.43	3.21	4.19	2.96
Step1X-Edit	7B+12B	3.88	3.14	3.40	2.41	3.16	4.63	3.06
ICEdit	12B	3.58	3.39	3.15	2.93	3.08	3.84	3.05
BAGEL	7B+7B	3.56	3.31	3.30	2.62	3.24	4.49	3.20
UniWorld-V1	7B+12B	3.82	3.64	3.47	3.24	2.99	4.21	3.26
Janus-4o	7B	3.60	3.25	3.27	2.28	3.32	4.47	3.26
OmniGen2	3B+4B	3.57	3.06	3.74	3.20	3.57	4.81	3.44
UniLIP-1B	1B+0.6B	4.11	3.58	4.30	3.97	4.00	4.87	3.81
MUSE-1B (Ours)	1B+0.6B	4.15	3.72	4.34	4.03	4.12	4.88	3.92
UniLIP-3B	2B+1.6B	4.29	3.90	4.44	4.10	4.14	4.80	3.94
MUSE-3B (Ours)	2B+1.6B	4.35	4.02	4.50	4.15	4.22	4.85	4.08

Table 8. **Computational Cost Comparison.** Parameters denote total active parameters during inference (Encoder + Connector + Decoder). MUSE achieves a comparable cost to the single-stream baseline while significantly outperforming the heavy two-stream paradigm. Throughput measured on H20 GPU (BS=48).

Method Architecture	Components (Example)	Active Params	Throughput
Two-Stream	VQGAN (Reconst.) + CLIP-L (Semantics)	~650M	~18 img/s
Naive Unified	UniLIP (InternViT + ResBlock Connector)	482M	32 img/s
MUSE (Ours)	InternViT + Synergistic Connector	496M	30 img/s
<i>Comparison</i>	<i>vs. Two-Stream</i>	<i>-23% Params</i>	<i>+66% Speed</i>

D.2. Complex Generation and Editing Scenarios

We showcase the robustness of MUSE in challenging scenarios: **Figure 9** demonstrates multi-turn editing, where the model must maintain consistency across sequential modifications. **Figure 8** displays text-to-image generation with dense caption inputs (over 100 tokens), highlighting the model’s ability to handle long-context semantic binding.

E. Implementation Details, Sensitivity, and Efficiency Analysis

E.1. Hyperparameter Settings

We provide the comprehensive hyperparameter configurations used for training the MUSE framework in Table 9. The training is conducted on 8 NVIDIA H20 GPUs. Note that for the *Spectral Gradient Filtering*, the coefficient λ_{spec} is critical; it is set to 0.1 to dampen high-frequency oscillation from the pixel reconstruction loss, protecting the semantic manifold.

E.2. Sensitivity Analysis

We investigate the sensitivity of MUSE to two key architectural hyperparameters: the codebook size/query number (N) and the depth of the connector.

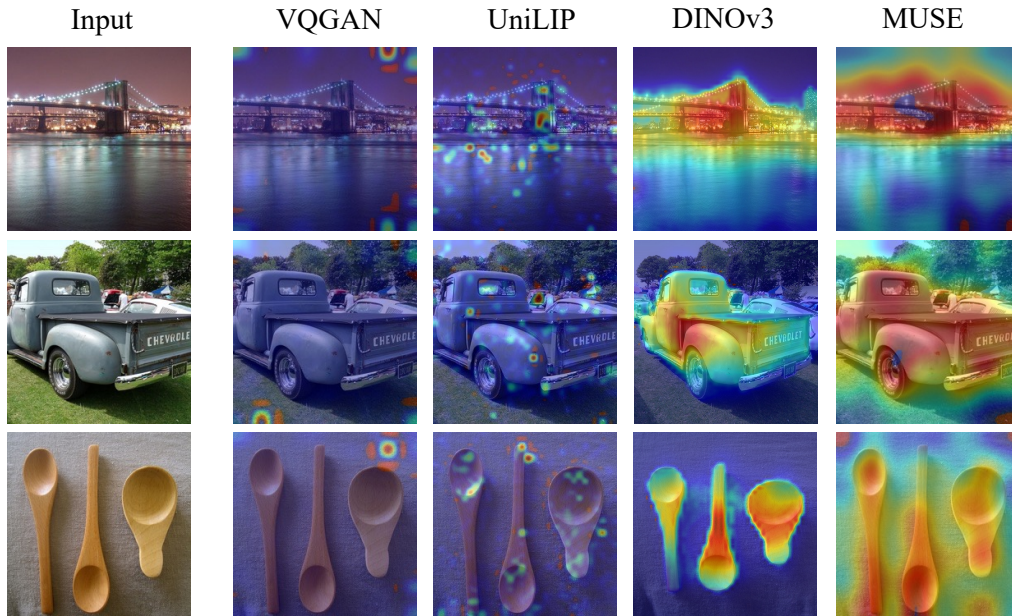


Figure 7. **Qualitative Comparison of Attention Topologies.** We visualize the [CLS] attention maps of the same image across different tokenizers. **VQGAN** fixates on local textures (e.g., fur details) but misses the object shape. **UniLIP** captures the rough location but lacks boundary precision. **MUSE (Ours)** achieves *DINO*-level object segmentation, precisely attending to the semantic subject while suppressing background noise.

Number of Queries (N). We varied the number of learnable queries $N \in \{64, 128, 256, 512\}$ to study the trade-off between compression rate and information density. As illustrated in Figure 10 (Left):

- **Reconstruction (rFID):** Improving monotonically as N increases, as more tokens allow for encoding higher-frequency spatial details.
- **Understanding (Zero-Shot Acc):** Performance peaks at $N = 256$. Notably, increasing N to 512 causes a slight degradation (77.1% \rightarrow 76.4%). We hypothesize that excessive token granularity introduces redundant background noise into the latent space, diluting the density of semantic concepts required for robust understanding. Thus, $N = 256$ represents the optimal Pareto point.

Connector Depth. We experimented with connector depths of $\{2, 4, 6, 8, 12\}$ layers within the UMM. Figure 10 (Right) reveals that a shallow connector (2 layers) creates an information bottleneck, failing to align the text-image modalities (MMB score \downarrow 60). Performance saturates at 6 layers. Utilizing deeper connectors (e.g., 12 layers) yields diminishing returns while linearly increasing inference latency. Consequently, we adopt a 6-layer MLP structure.

E.3. Computational Complexity and Efficiency Analysis

We conduct a rigorous efficiency analysis on $8 \times$ NVIDIA H20 GPUs (global batch size 48). We compare MUSE against the naive unified baseline (UniLIP) and the traditional two-stream paradigm.

Marginal Cost for Structural Synergy. While MUSE introduces specialized mechanisms to resolve manifold misalignment, the computational overhead remains minimal:

- **Parameter Overhead:** Compared to the UniLIP baseline (482M), MUSE (496M) increases parameters by only $\sim 2.9\%$. This slight increase comes from the projection layers in the *Synergistic Block* necessary to physically decouple semantic and topological gradients.
- **Throughput Trade-off:** The inference throughput of MUSE is **30 img/s**, compared to 32 img/s for UniLIP. We argue that this **6% latency cost** is a negligible price to pay for breaking the "Zero-Sum Game" between generation and



Figure 8. Qualitative comparison of text-to-image generation.

understanding. UniLIP achieves its speed by sacrificing semantic robustness (as shown in Table 1), whereas MUSE maintains omnipotent capabilities.

Superiority over Functional Equivalents. To achieve a “functionally equivalent” system to MUSE (i.e., one that possesses both high-fidelity generation and specialist-level understanding) using standard methods, one would typically resort to a two-stream approach (e.g., running VQGAN + CLIP-Large in parallel). As shown in Table 8, compared to this functional equivalent, MUSE offers a $1.6\times$ speedup and reduces memory footprint by 23%, proving it is the most efficient path to omnipotent multimodal intelligence.

More broadly, the design philosophy of MUSE is consistent with recent efforts toward building efficient, unified, and controllable AI systems across diverse domains, where representation quality, computational efficiency, and task adaptability are jointly emphasized. These trends have appeared in digital twin and smart manufacturing systems (Ren et al., 2025), video-language and robotic manipulation models (Li et al., 2025b; 2026b), recommender-system unlearning (Li et al., 2025d; 2023), human motion understanding (Jia et al., 2026; Li et al., 2025a; 2026a), prompt optimization and architecture search (Xiang et al., 2025; Liang et al., 2025; Kong et al., 2025; 2023), efficient reasoning and tool-using language models (Jiang & Ferraro, 2026a; Jiang et al., 2025; Xu et al., 2025; Zhang et al., 2025; Jiang & Ferraro, 2026b), as well as lightweight forecasting, visual recognition, and task-specific language modeling (Li et al., 2025c; 2026c; 2024c; Cao et al., 2026; Yang et al., 2026c;a;b). From this perspective, our exploration of topological orthogonality provides one possible instance of a more general principle: separating conflicting factors in representation learning can improve both efficiency and downstream generalization.

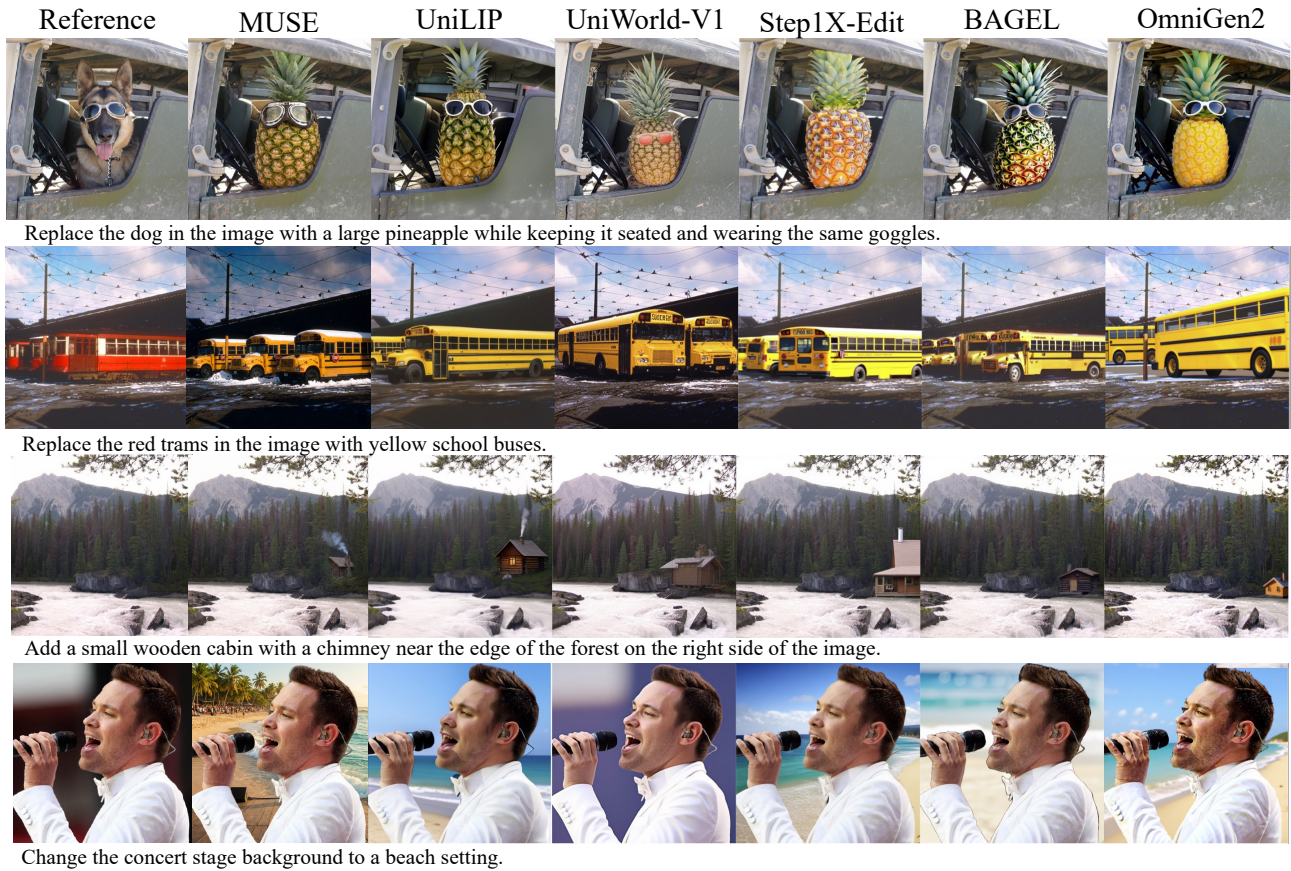


Figure 9. Qualitative comparison of image editing.

Table 9. Detailed Hyperparameter Configurations. The three-stage training ensures progressive alignment from topology to semantics to full synergy.

Hyperparameter	Stage 1: Topology	Stage 2: Semantic	Stage 3: Synergy
Optimizer	AdamW	AdamW	AdamW
Global Batch Size	384	384	384
Learning Rate (Peak)	$4e^{-4}$	$2e^{-4}$	$1e^{-5}$
Min Learning Rate	$1e^{-5}$	$1e^{-5}$	$1e^{-6}$
Weight Decay	0.05	0.05	0.05
Warmup Steps	2000	2000	5000
Input Resolution	224^2	224^2	$224^2 \rightarrow 448^2$
<i>Loss Weights</i>			
λ_{topo} (Topology)	1.0	1.0	1.0
λ_{anchor} (Semantic)	-	0.2	0.1
λ_{rec} (Reconstruction)	-	-	1.0
λ_{spec} (Gradient Scale)	-	-	0.5
λ_{gan} (Adversarial)	-	-	0.1 (starts at 5k steps)

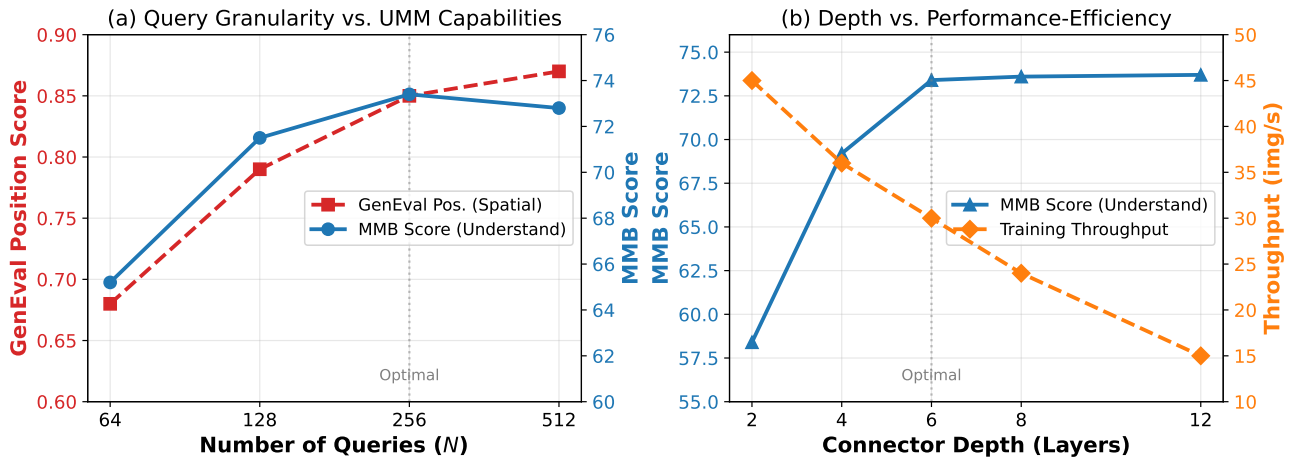


Figure 10. **Sensitivity Analysis.** (Left) Impact of query number N . While reconstruction improves with more tokens, semantic understanding peaks at 256, suggesting a "Semantic Density" limit. (Right) Impact of connector depth on Multimodal Benchmark (MMB) performance and training throughput.